ELSEVIER

Fluid Dynamics Research 34 (2004) 273–288

FLUID DYNAMICS RESEARCH

Verification and validation studies of the time-averaged velocity field in the very near-wake of a finite elliptical cylinder

Michael R. Flynn[a,*], Alfred D. Eisner[b]

[a] *Department of Environmental Sciences and Engineering, University of North Carolina, 104 Rosenau Hall, Chapel Hill, NC 27599-7400, USA*

[b] *Mantech Environmental Technology, Inc., RTP, NC 27709, USA*

Received 6 June 2003; received in revised form 2 February 2004; accepted 4 February 2004
Communicated by E. Knobloch

Abstract

This paper presents verification and validation results for the time-averaged, three-dimensional velocity field immediately downstream of a finite elliptic cylinder at a Reynolds number of 1.35×10^4. Numerical simulations were performed with the finite element package, Fidap, using the steady state, standard k-epsilon model. The ratio of the cylinder height to the major axis of the elliptical cross section is 5.0; the aspect ratio of the cross section is 0.5625. This particular geometry is selected as a crude surrogate for the human form in consideration of further applied occupational and environmental health studies. Predictions of the velocity and turbulence kinetic energy fields in the very near-wake are compared to measurements taken in a wind tunnel using laser Doppler anemometry. Results show that at all locations where a reliable grid convergence index can be calculated there is not a demonstrable difference between simulated and measured values. The overall topology of the time-averaged flow field is reasonably well predicted, although the simulated near-wake is narrower than the measured one.

Keywords: Numerical simulation; Verification and Validation; Finite elliptical cylinder

1. Introduction

Many important fluid dynamic problems involve three-dimensional, separated flow around bluff bodies. One specific application is estimating human exposure to airborne contaminants and the

* Corresponding author. Tel.: +1-919-966-3473; fax: +1-919-966-7911.
E-mail address: mike_flynn@unc.edu (M.R. Flynn).

0169-5983/$30.00
doi:10.1016/j.fluiddyn.2004.02.001

associated control problem using local exhaust ventilation (Flynn and Sills, 2000). Real-world scenarios are complex and include time-dependent, three-dimensional, effects with moving boundaries. At present computational resources are inadequate to simulate such problems completely. Most simulations involve simple geometry with steady Reynolds averaged Navier–Stokes (RANS) models using the standard k-epsilon turbulence closure (Flynn and Sills, 2001; Heinonen et al., 1996; Kulmala et al., 1996) or the RNG k-epsilon model (Hyun and Kleinstreuer, 2002). A few two-dimensional, time-dependent, direct numerical simulations have employed discrete vortex methods for these types of problems (Flynn et al., 1995; Kim and Flynn, 1995).

The near-wake that forms downstream of the human body immersed in airflow is an important determinant of exposure to toxic airborne contaminants (Kim and Flynn, 1991; Flynn and Ljungqvist, 1995). Re-circulation of air in this region is critical in determining the transport of pollutants into the breathing-zone. Under certain conditions this flow is periodic and may involve vortex shedding. However, the use of unsteady simulations to capture such a phenomenon in three-dimensions is prohibitive since the time scale of shedding is small compared to the interval over which the integration would need to take place. In addition, a recent, direct numerical simulation of the wake of a two-dimensional circular cylinder, Ma et al. (2000), suggests that the very near wake (less than 3 diameters downstream) may be less influenced by vortex shedding and more by the character of the separating shear layers.

Although steady RANS models have limitations, it is clear they can capture some of the critical features of the time-averaged wake behind a two-dimensional circular cylinder. A review of existing studies suggests that for three-dimensional problems, and for many two-dimensional problems, insufficient verification studies have been performed to indicate the adequacy, or lack thereof, for RANS models to characterize the very near-wake flow field. A recent study (Richmond-Bryant, 2003) indicates that while the standard and RNG k-epsilon models predict delayed boundary layer separation on the two-dimensional, circular cylinder, they do capture the time-averaged re-circulation bubble. The length of the bubble is in reasonable agreement with experimental data, but the predicted width is narrower than measurements indicate. There was very little difference between predictions for either turbulence model.

The human form is arguably more elliptic in cross section, and the sharper radius of curvature at the shoulder of the ellipse may help alleviate the delayed separation problems observed with RANS models for the two-dimensional circular cylinder noted above. The finite elliptical cylinder is thus selected here as a three-dimensional benchmark flow for further, more realistic, human exposure studies. The geometric limitations are obvious, but the separated flow field is of fundamental significance. The primary goal in this paper is to explore the computational resources necessary to verify the predictions of the three-dimensional, time-averaged velocity field in the very near-wake, and to explore validation with laser Doppler velocity measurements.

As used here the term validation should not be construed to indicate that a steady RANS simulation would be adequate to capture all the flow dynamics for this problem. Our interest is in validating the predictions of the time-averaged values of velocity and turbulence kinetic energy in the immediate near wake. Ultimately numerical studies of contaminant transport in this region will provide the information necessary to judge the adequacy of the velocity field and the overall approach. Prior to embarking on those studies, however, a well-characterized velocity field is needed.

Although numerical (Chandna, 1997) and experimental (Kondjoyan and Daudin, 1995) studies on cylinders of elliptic cross section have been performed, they are either two-dimensional or focus on

heat and mass transfer from the cylinder surface. Near-wake studies at the Reynolds numbers of interest and the geometry of concern here have not, to our knowledge, been examined. The most relevant literature would appear to be for circular cylinders of finite height.

The wind tunnel study of Okamoto and Sunabashiri (1992) presents hot wire anemometry data for flows past circular cylinders with various height-to-diameter ratios, (H/D) at Reynolds numbers from 25,000–47,000. While they focus on time-dependent vortex shedding, a time-averaged re-circulation region is also presented. Tanaka and Murata (1999) present time-averaged velocities in the far-wake of circular cylinders with H/D ratios of 1.25–10, at a Reynolds number of 37,000. They used a novel Pitot tube to get three-dimensional velocities, however measurements in the very near-wake were not possible. More recently, Park and Lee (2000) used a hot wire anemometer to examine the flow near circular cylinders with H/D ratios of 5–13 at Reynolds number 20,000. They focused on vortex shedding at the free-end of the cylinder, and also presented flow visualizations of the near-wake region.

Verification and validation studies are currently of great interest in the CFD community, and are evolving into consensus-based processes, although clearly there are still many unresolved issues. For the verification studies reported here we follow the guidance provided by three primary references (Stern et al., 2000; Roache, 1998; Cadafalch et al., 2002), and focus on the two major sources of error: non-linear iteration and mesh convergence. The goal is to identify those points in the very near wake where measurements were made and where a reliable grid convergence index can be calculated to estimate numerical uncertainty. Those points are then examined for validation, defined here as an overlap between the numerical and experimental uncertainty intervals.

2. Methods

The three-dimensional air velocity field downstream of a finite elliptical cylinder was simulated numerically using Fidap v. 8.6.2 and subsequently measured using laser Doppler anemometry in a wind tunnel. The cylinder was 0.86 m tall, and the cross sectional ellipse had major and minor axes of 0.172 and 0.09675 m, respectively. The cylinder was oriented such that the major axis of the cross section was perpendicular to the freestream velocity. The Reynolds number based on the major axis as the length scale was approximately 13,500 and within the range typically experienced in occupational settings. Fig. 1 shows the geometry, co-ordinate system, and nomenclature for this problem. The Cartesian co-ordinates of the center of the elliptical cylinder in the base plane are (0.75, 0.0, 0.0). Numerical and experimental details are given below.

2.1. Numerical

The equations selected to model the airflow are the steady state, incompressible, turbulent, Navier–Stokes equations

$$\nabla \cdot \mathbf{u} = 0, \tag{1}$$

$$\mathbf{u} \cdot \nabla \mathbf{u} = \nabla \cdot \left[\frac{\mu + \mu_t}{\rho} (\nabla \mathbf{u} + \nabla \mathbf{u}^{\mathrm{T}}) \right] - \frac{1}{\rho} \nabla_p. \tag{2}$$

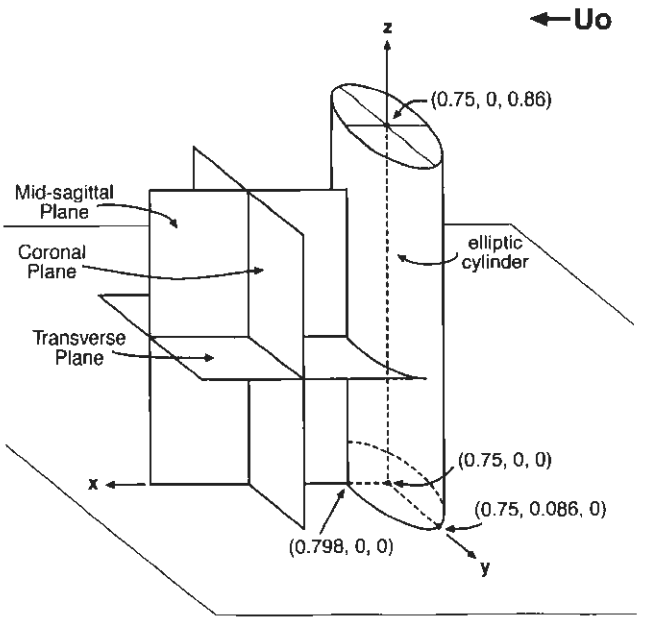

Fig. 1. The geometry and co-ordinate system for the elliptical cylinder.

The Boussinesq constitutive relationship is used to model the Reynolds stresses, and the eddy viscosity is

$$\mu_t = \rho c_\mu \frac{k^2}{\varepsilon}. \tag{3}$$

The k-epsilon equations for turbulence kinetic energy and dissipation are

$$\rho(\mathbf{u}\cdot\nabla k) = \nabla\cdot\left(\mu + \frac{\mu_t}{\sigma_k}\nabla k\right) + \frac{\mu_t}{\mu}\Phi - \rho\varepsilon, \tag{4}$$

$$\rho(\mathbf{u}\cdot\nabla \varepsilon) = \nabla\cdot\left(\mu + \frac{\mu_t}{\sigma_\varepsilon}\nabla \varepsilon\right) + c_1\frac{\varepsilon}{k}\frac{\mu_t}{\mu}\Phi - c_2\rho\frac{\varepsilon^2}{k}. \tag{5}$$

Here, Φ is the viscous dissipation function and

$$c_\mu = 0.09, \quad \sigma_k = 1.00, \quad \sigma_\varepsilon = 1.30, \quad c_1 = 1.44, \quad c_2 = 1.92.$$

The computational domain and boundary conditions are selected to match the wind tunnel experiment, as closely as possible. Due to symmetry only one half of the physical domain is modeled. Three different mesh densities ($M1$, $M2$, and $M3$) were employed containing approximately 193,000, 337,000, and 521,000 total elements, respectively. All meshes were generated using the FIGEN process in Fidap (Fluid Dynamics International, 1998). The number of elements on the mesh edges was increased by a constant proportion to give a mesh-coarsening factor, r, of approximately 1.2. Fig. 2 illustrates the computational domain for the coarsest mesh level ($M1$).

On the inlet a uniform velocity of 1.2 m/s with turbulence kinetic energy of 0.00346 m^2/s^2 and dissipation of 0.007 m^2/s^3 are specified. These values were selected based on the experimental

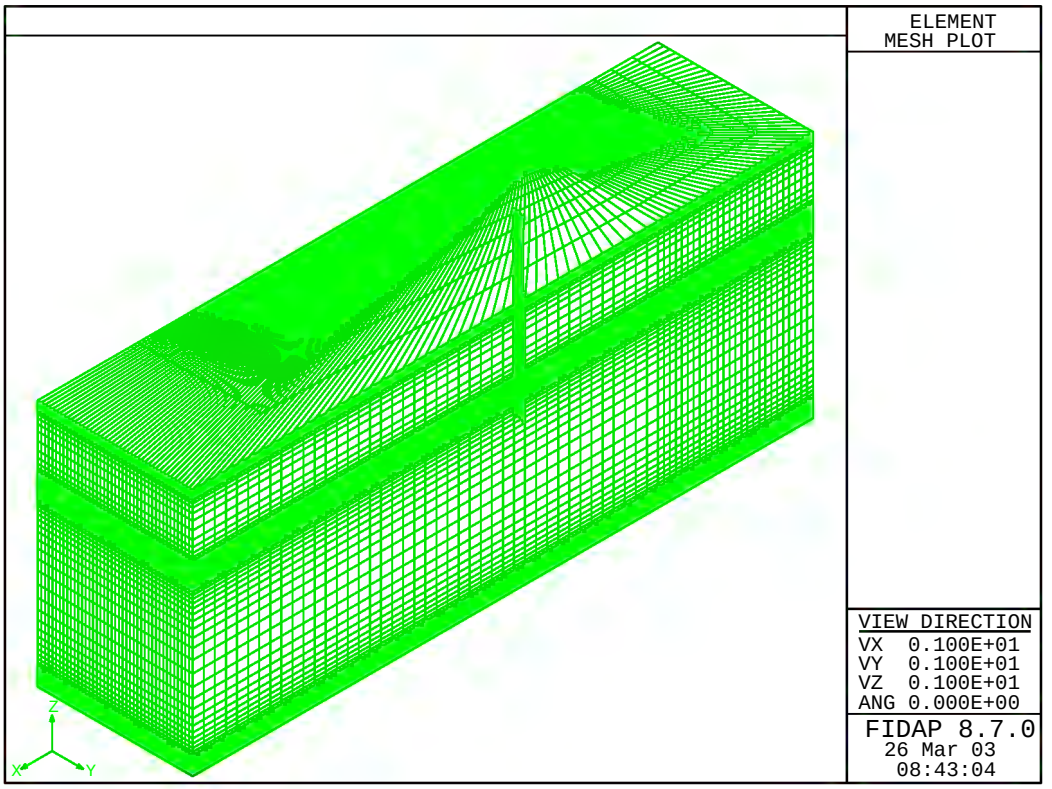

Fig. 2. The computational domain—mesh level $M1$.

measurements of turbulence intensity with the assumption that the ratio of eddy viscosity to laminar viscosity was on the order of ten. A sensitivity analysis of the results to the inlet flow conditions was not conducted, as it was not thought to be a major factor in the uncertainty. The outlet is specified as a no-stress boundary, the walls and cylinder surface are no-slip, and the symmetry plane has zero normal velocity and zero tangential stress. The outlet boundary was placed downstream of the cylinder at a distance thought to be sufficiently far from the cylinder so that the velocity field would recover and the no-stress condition would be reasonable, this distance was selected based on the experimental work of Tanaka and Murata (1999).

The simulations were conducted using the segregated solver with pressure projection and an element-Reynolds number relaxation scheme. Streamline-upwinding was used to stabilize the convective terms. This form of upwinding is very nearly second-order accurate with no crosswind artificial dissipation. The iterative solvers for the linear systems were the conjugate gradient squared and conjugate residual methods.

2.2. Experimental

Experimental work was conducted in a closed-loop wind tunnel with a centrifugal blower powered by a 50-hp motor. The tunnel test-section measures 1.52 m wide by 1.22 m high and 0.7 m in

length. The bypass section of the tunnel contains a fan used for low wind speeds (typically less than 0.5 m/s).

Flow quality in the wind tunnel at low wind speeds was investigated (Eisner et al., 2002) and improved. In order to straighten the flow and decrease the turbulence levels, a flow-straightening honeycomb is used in the wind tunnel at the junction between the contraction and the test section. This honeycomb has a cell size of approximately 0.5 cm, a cell wall thickness of 0.02 cm, and a depth in the flow direction of 10 cm. The flow uniformity at a tunnel wind speed of 1.0 m/s was measured using laser Doppler velocimetry and a fog generator (Heist et al., 2003). Measurements outside the wall boundary layers were within ±4.5% of the average velocity.

Velocity measurements were made using a phase Doppler anemometry (PDA) system. The system is capable of performing simultaneous velocity and particle size measurements, although only the velocity measuring capability laser Doppler anemometry (LDA) was used for this work. A theatrical fog generator (Magnum Pro 2000, Martin Manufacturing PLC, Louth, UK) was used to seed the flow for the measurements.

The PDA employed in this study used a Coherent Innova 300 argon-ion laser to supply the laser light. The beam was separated into at least six colors with three being used, including wavelengths 514.5 nm (green), 488.0 nm (blue), and 476.5 nm (violet). The beam is separated using a Dantec FiberFlow optical system, which includes beam-splitting and frequency-shifting devices and fiber manipulators for guiding the laser beams into optical fibers. In the FiberFlow unit, each of the three beams is split into two. One of each of these pairs passes through a Bragg cell and frequency is shifted by 40 MHz. Frequency shifting is used to eliminate the ambiguity in the direction of the measured velocity. The signals from the photomultiplier tubes are analyzed with PDA signal processor (Model 58N10, Dantec Dynamics, Slovlunde, Denmark). Due to beam blockage by the floor of the tunnel, velocity measurements were not possible at a distance from the floor of less than 25 cm.

Three-dimensional, time-averaged and fluctuating velocity components were measured in the near wake of the cylinder located in the wind tunnel. The blockage ratio for the elliptical cylinder in the test section was approximately 8.0%. Air velocity measurements were taken at approximately 4000 locations distributed on seven planes defined by different elevations (z co-ordinate). Incremental spacing in the x–y directions was 0.025 m. Measured velocities on both sides of the cylinder axis of symmetry were made and served as replicate measurements for comparison to the model predictions. A total of 2000 point measurements were thus obtained. This required reflecting the y velocity components from one of the measurement planes to keep the correct sign. The fluctuating velocity components were used to calculate experimental turbulence kinetic energy.

3. Experimental results

The experimental data (u, v, w and k) are summarized by a mean and standard deviation based on the two replicates for each of the 2000 points. Standard deviations were corrected to account for only two replicates, (Sokal and Rohlf, 1981). In a small subset of the data four replicates were made when it was necessary to realign traversing optics. In these cases the two replicates used in the analysis were the means of the measurements from each side of the ellipse, in all other cases the replicates were in fact the measurements from each side. Although there is some lack of

Table 1
Ranges and fraction of measurements below indicated multiple of c.v.

	Max, Min	< 0.1 c.v.	< 0.25 c.v.	< 1.0 c.v.
U	1.3, −0.28 (m/s)	0.66	0.83	0.96
V	0.32, −0.30 (m/s)	0.20	0.35	0.67
W	0.44, −0.37 (m/s)	0.32	0.54	0.85
K	0.18, 0.0003 $(m/s)^2$	0.33	0.67	0.99

independence in this approach it is not expected to impact the analysis significantly and it was a reasonable trade-off to feasibly acquire the data.

Table 1 presents the maximum and minimum measured values for each degree of freedom. In addition the fraction of measurements with coefficients of variation (c.v.) less than 0.1, 0.25, and 1.0 are also presented. The data indicate that the x-component of velocity and the turbulence kinetic energy were measured most precisely, while the y-velocity component had the greatest experimental variability. This was not unexpected as the y-velocity component was often near zero.

4. Verification

Verification studies proceeded sequentially. For each of the three meshes non-linear iterative convergence was established, followed by an assessment of the mesh convergence. Local observed orders of accuracy were then calculated at all points that showed monotonic convergence. Grid convergence indices were subsequently calculated at each point that showed an observed order of accuracy within the theoretical limits of the numerical method (between 1 and 2). This information was used to estimate numerical uncertainty for the validation studies.

4.1. Non-linear convergence

The Fidap software provides a global "solution" error norm to monitor non-linear convergence. This is the traditional relative L_2 error norm calculated for each degree freedom at all nodes of the mesh. The default criterion for the segregated algorithm is simultaneous convergence for all degrees of freedom to less than 10^{-3}. To assess the adequacy of this level for the 2000 points in the near wake an order of magnitude reduction to 10^{-4} was achieved and a relative L_2 error norm calculated for the 2000 points at the two levels of iterative convergence. This process of lowering the global solution error tolerance by an order of magnitude and then examining the relative changes at the 2000 points was repeated until negligible differences were observed. The local relative L_2 error norm for the 2000 points was $< 5\%$ and plots indicated no discernible differences between the two levels. This led to confidence that the non-linear errors would be small relative to any of the mesh errors. Global solution error norms needed to be reduced to O (10^{-5}–10^{-6}) to achieve this level of local accuracy at the 2000 points.

Table 2
Global mesh convergence ratios, R (at various levels of non-linear convergence; GSE=global solution error)

	u	v	w	p	k	e
R (GSE $< 10^{-3}$)	1.5	1.0	1.2	1.25	1.3	1.25
R (GSE $< 10^{-4}$)	0.52	0.63	0.44	0.84	0.59	0.53
R (GSE $< 10^{-5}$)	0.57	0.64	0.44	0.87	0.59	0.55

4.2. Mesh convergence (truncation)

After iterative convergence was established for each mesh a global convergence ratio, R, was calculated for each degree of freedom based on the L_2 error norm for all 2000 points, as defined below

$$R = \frac{\|\varepsilon_{2,3}\|_2}{\|\varepsilon_{1,2}\|_2} \quad \text{where } \|\varepsilon\|_2 = \sqrt{\sum_{i=1}^{2000} \varepsilon_i^2} \tag{6}$$

In Eq. (6) $\varepsilon_{j,k}$ is the difference between the coarser and finer mesh level values for the degree of freedom in question.

Table 2 shows that at the highest level of iterative convergence each degree of freedom has a global convergence ratio between 0 and 1 indicating monotonic convergence. Note that at the default level for iterative convergence (G.S.E.=0.001) all R-values indicate divergence and the inadequacy of the default tolerance. Unfortunately the global convergence ratio, R, obscures local information (see e.g., Stern et al., 2001), and can mask local divergent and/or oscillatory conditions. Therefore a convergence ratio is calculated locally for each degree of freedom at each of the 2000 points. Results indicated that of the 12,000 possible local convergence ratios, 17% were divergent, 48% exhibited oscillatory convergence, and 32% exhibited monotonic convergence. The remaining 3% were considered converged nodes, ($|R| < 10^{-16}$).

For monotonically convergent nodes, a local observed order of accuracy (p) was calculated according to

$$p = \frac{\ln(\varepsilon_{1,2}/\varepsilon_{2,3})}{\ln(r)}. \tag{7}$$

A wide range of p values was obtained and only a small percentage exhibited values within the theoretical order of accuracy for the method, i.e., $1 < p < 2$. For these particular locations, and degrees of freedom, a reliable absolute grid convergence index (G.C.I.) (Roache, 1998) is calculated as

$$\text{G.C.I.} = 1.25 \left| \frac{\varepsilon_{2,3}}{r^p - 1} \right|. \tag{8}$$

This was subsequently used to define the limits of numerical uncertainty.

A more heuristic approach to verification was also employed. For all 2000 points and for each degree of freedom 2 least squares regressions were performed. The first plotting mesh 1 results vs. mesh 2 and finally mesh 2 vs. mesh 3. If the results are converging the slopes and intercepts

Table 3
Verification regression statistics

Degree of freedom	Slope	Slope 95% C.I.	Intercept	Intercept 95% C.I.	Coefficient of determination
U (1 vs. 2)	0.976	[0.971,0.980]	0.054	[0.048,0.058]	0.988
U (2 vs. 3)	0.991	[0.993,0.998]	0.034	[0.032,0.037]	0.997
V (1 vs. 2)	0.929	[0.904,0.955]	−0.012	[−0.014,−0.01]	0.718
V (2 vs. 3)	0.945	[0.927,0.961]	−0.007	[−0.009,−0.006]	0.861
W (1 vs. 2)	1.088	[1.075,1.10]	−0.007	[−0.009,−0.005]	0.933
W (2 vs. 3)	1.025	[1.019,1.03]	0.0006	[−0.003,0.0016]	0.982
P (1 vs. 2)	1.007	[1.003,1.01]	0.009	[0.008,0.0098]	0.992
P (2 vs. 3)	1.005	[1.002,1.007]	0.010	[0.0098,0.011]	0.996
K (1 vs. 2)	0.969	[0.955,0.983]	0.0008	[−0.0002,0.002]	0.902
K (2 vs. 3)	1.003	[0.995,1.011]	−0.0015	[−0.002,−0.001]	0.963
E (1 vs. 2)	1.016	[1.003,1.03]	0.003	[−0.0007,0.007]	0.917
E (2 vs. 3)	0.998	[0.991,1.006]	−0.0003	[−0.003,0.002]	0.971

of such regressions should approach 1.0 and 0.0, respectively, and the coefficient of determination, (R^2) should approach 1.0. Table 3 presents the results of these regressions. In all cases the slopes, intercepts, and R^2 values approach the ideal values with increasing mesh refinement. The greatest residual errors occur with the y-component of velocity. This approach characterizes all errors in a statistical sense and the coefficients of determination indicate that there is very little uncertainty left to explain with continued numerical refinement. A subjective assessment is that a good degree of "mesh independence" is demonstrated.

5. Validation

Validation is considered to have occurred here when the numerical and experimental uncertainty intervals overlap. The uncertainty around the numerical prediction from the finest mesh, ($M3$), is plus or minus the grid convergence index. The experimental uncertainty is plus or minus the standard deviation of the measurement. For all points and degrees of freedom that had an observed order of accuracy within the theoretical limits of the method, validation was achieved. This was significant in that for points where a reliable estimate of the numerical uncertainty could be made, no distinction could be made with the experimental data.

For locations with monotonic convergence, but observed orders of accuracy outside the theoretical limits of the method, an additional analysis was performed. Correlation coefficients were calculated between measured and predicted values and the percentage of points where the simulated value was within the measured value plus or minus two standard deviations was determined. This information

Table 4
Fraction of numerical predictions within the indicated experimental uncertainty for locations with monotonic convergence, but observed orders of accuracy outside the theoretical limits

Degree of freedom (N)	Mean $\pm\,\sigma$	Mean $\pm\,2\sigma$	Mean $\pm\,3\sigma$	Correlation coefficient
U (589)	0.23	0.38	0.48	0.90
V (487)	0.56	0.75	0.82	0.90
W (659)	0.28	0.45	0.57	0.85
K (535)	0.28	0.45	0.59	0.77

The last column contains the correlation coefficients between measured and predicted degrees of freedom.

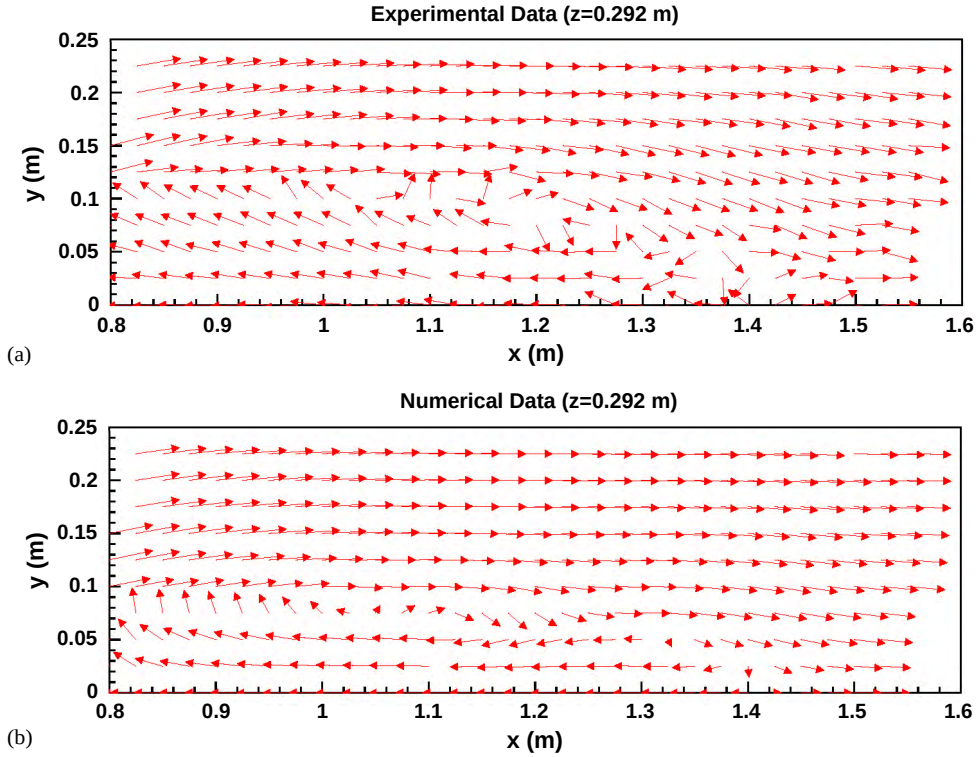

Fig. 3. Measured (a) and numerical (b) velocity vectors in the transverse plane at $z = 0.292$ m.

is reported in Table 4 and provides some further assessment of the models performance although clearly not of the same quality as the data above.

Experimental and numerical comparisons for the velocity components are displayed as vector plots in Figs. 3–6. Each figure shows the experimental and associated model predictions on the finest mesh ($M3$). The qualitative picture of the near wake is similar for both model and experiment. A time averaged re-circulation bubble is present and can be seen in the transverse planes at two different elevations (Figs. 3 and 4), and to some degree in the mid-sagittal plane of symmetry, Fig. 5.

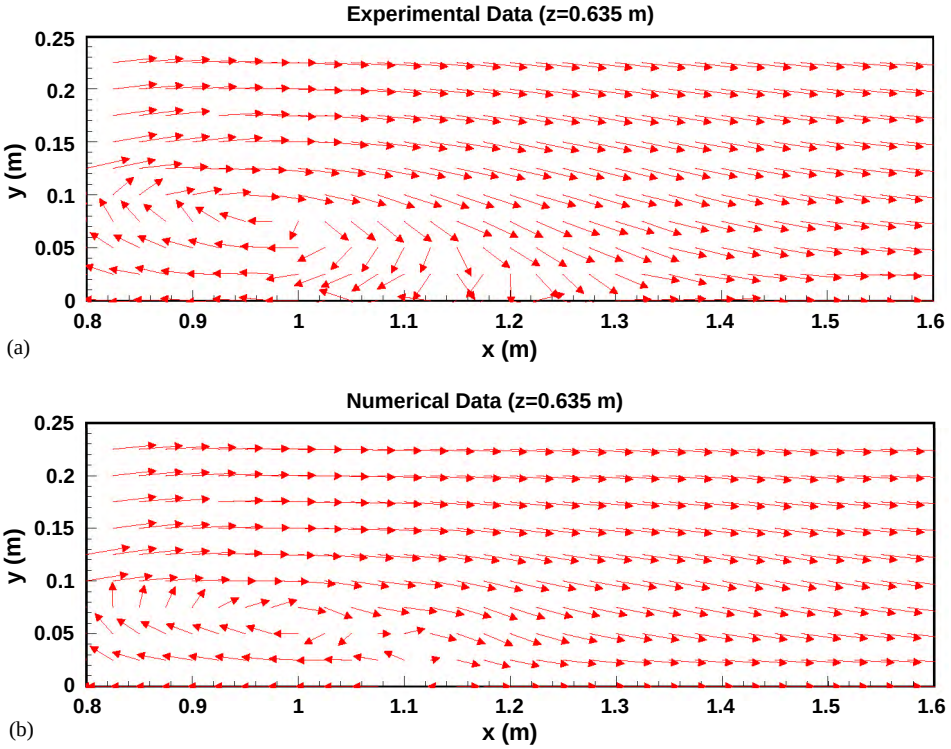

Fig. 4. Measured (a) and numerical (b) velocity vectors in the transverse plane at $z = 0.635$ m.

In the coronal (y–z) plane at $x = 1.0$ m (Fig. 6) an eddy spinning with the axis of rotation parallel to the freestream is evident. In Figs. 3a and 4a some of the y velocity components on the axis of symmetry are not zero as expected, this is most likely due to asymmetry in the cylinder itself and perhaps to some minor realignment errors.

These flow patterns are in good qualitative agreement with results for comparable finite circular cylinders cited earlier (Okamoto and Sunabashiri, 1992; Tanaka and Murata, 1999; Park and Lee, 2000). In general, the model predictions of re-circulation bubble length, seen in the transverse planes are in reasonable agreement with the experimental results. In the mid-sagittal plane the model predicts a thicker layer of vertical flow adjacent to the downstream side of the cylinder (Fig. 5b) than is shown in the experimental data (Fig. 5a).

The agreement between all measured and simulated data is illustrated in Figs. 7–10. In each plot the diagonal line indicates perfect agreement. There is considerable variation for each degree of freedom and some clear biases as well. The tendency for the model to over-predict the x-velocity component at the higher end of the range, shown in Fig. 7, is consistent with the narrow wake observed in Figs. 3b and 4b above. The measured z-velocity component is greater than the predicted value at the higher magnitudes (extremes of the plot in Fig. 9). This is consistent with the numerical data in Fig. 5b above showing the thickened boundary layer adjacent to the downstream side of the cylinder predicted by the model, while the measurements in Fig. 5a show a much

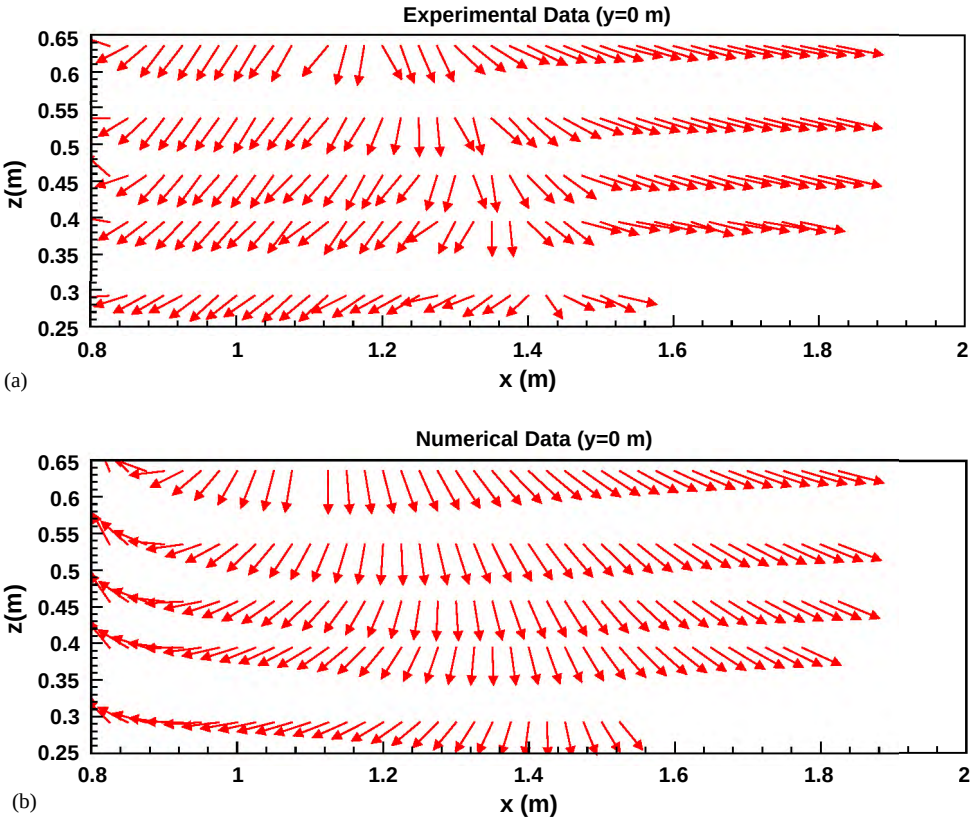

Fig. 5. Measured (a) and numerical (b) velocity vectors in the mid-sagittal plane, $y = 0$ m.

thinner layer. Turbulence kinetic energy varied widely as shown in Fig. 10 but no discernible bias is evident.

6. Concluding remarks

The numerical algorithm used here is reported to be nearly second-order accurate. The use of streamline upwinding to stabilize the convective terms will introduce some numerical diffusion in the direction of flow but not in the crosswind direction. The theoretical order of accuracy thus should be close to 2. However, the observed orders of accuracy were in many cases above or below this value, presumably due, in part, to the irregular mesh generated using the paving algorithm. This limited the number of locations at which reliable grid convergence indices could be calculated.

At locations where reliable grid convergence indices could be calculated no discernible difference between the predicted and measured values could be made. At locations that exhibited monotonic convergence, but had observed orders of accuracy outside the theoretical bounds, reasonable correlation existed between the measured and predicted values. However, for most of these cases, about half of the predicted values were outside the measured mean plus or minus three standard deviations.

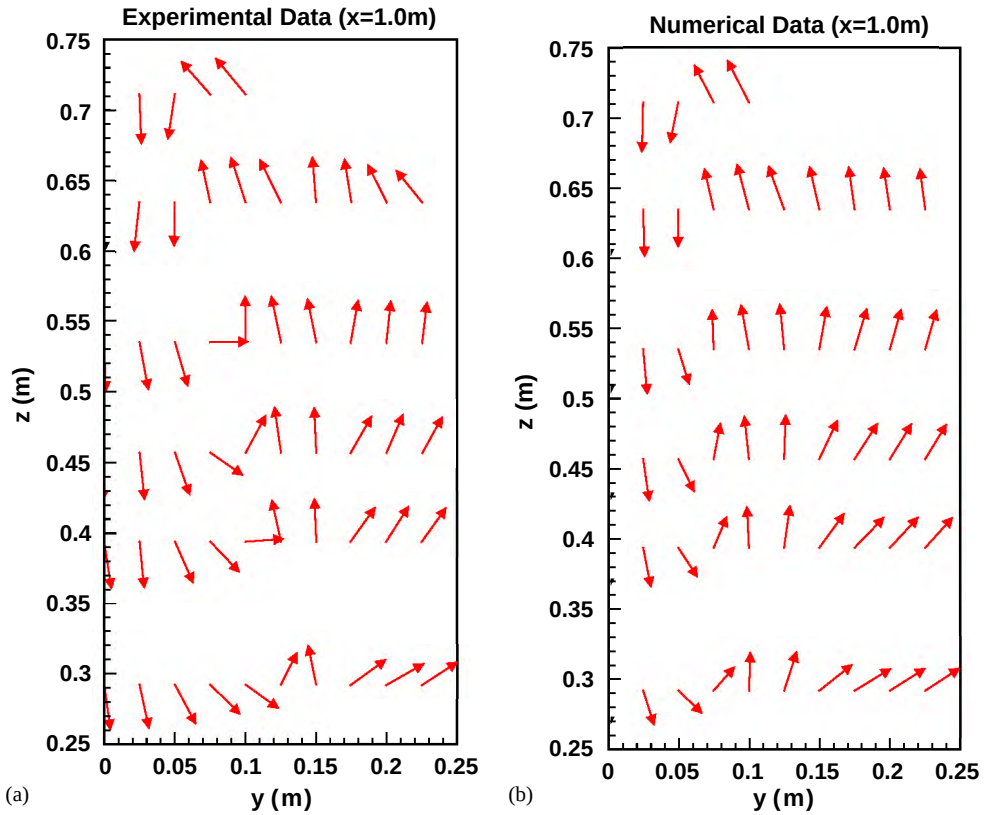

Fig. 6. Measured (a) and numerical (b) velocity vectors in the coronal plane at $x = 1.0$ m.

The figures indicate that while the predicted stagnation points on the various planes are in reasonable agreement with the measured values, the simulated re-circulation zones tend to be narrower than the corresponding measurements indicate.

These results suggest that on the order of a half million elements are required to begin to demonstrate a verified numerical solution for the near wake region. In addition, the non-linear iterative error, as indicated by the Fidap global solution norm, must be reduced to $O(10^{-5}–10^{-6})$ for all degrees of freedom simultaneously. The validation studies suggest that at quantifiable levels of uncertainty, no distinguishable differences can be made between model predictions and measured values. At many locations in the near wake no conclusions regarding validation can be drawn.

Due to the great variability in human exposure to airborne contaminants, and to the complexity of the governing airflow, current CFD simulations for these problems are limited. Discriminating the capability of RANS models to capture fluid flow phenomena relevant to human exposure is an important goal in assessing the utility of such simulations. Results presented here suggest that the standard k-epsilon model can predict a reasonable time-averaged velocity field in the very-near wake of a finite cylinder with elliptic cross-section at a Reynolds number of interest for human exposure problems.

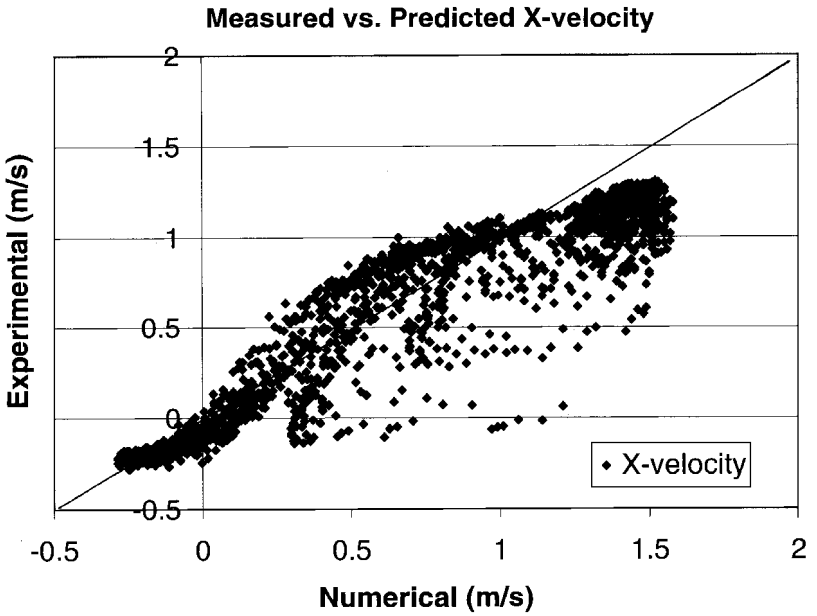

Fig. 7. Experimental vs. numerical results for the x-velocity component.

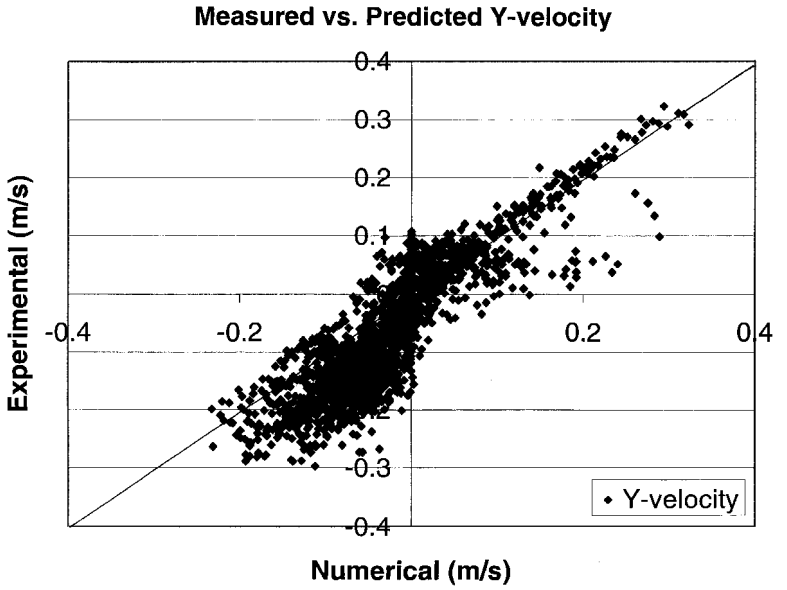

Fig. 8. Experimental vs. numerical results for the y-velocity component.

Although there are more advanced and accurate numerical methods for flows around bluff bodies, ultimately the complexity of the work environment will require methods flexible enough to capture a wide variety of fluid flow phenomena. Further research is underway to determine if the inaccuracies shown here will be significant limitations in simulations of contaminant transport and human exposure.

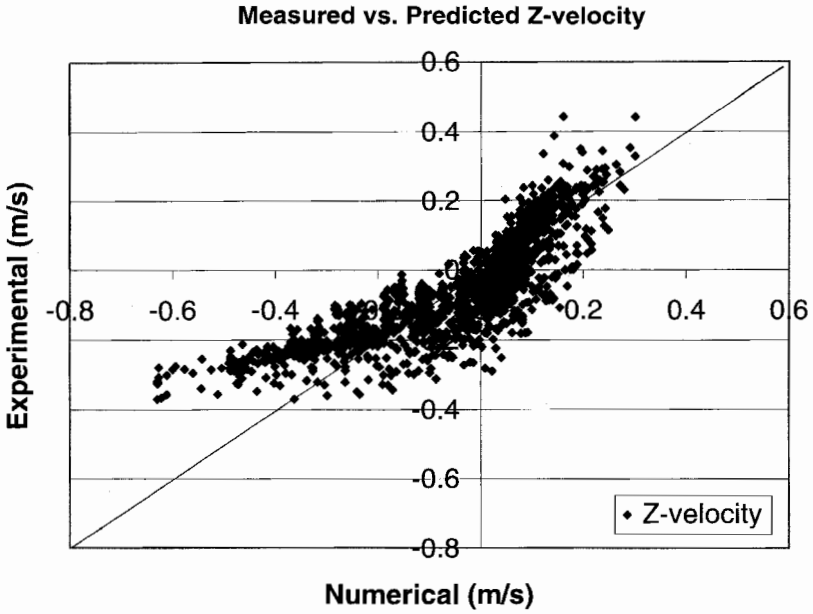

Fig. 9. Experimental vs. numerical results for the z-velocity component.

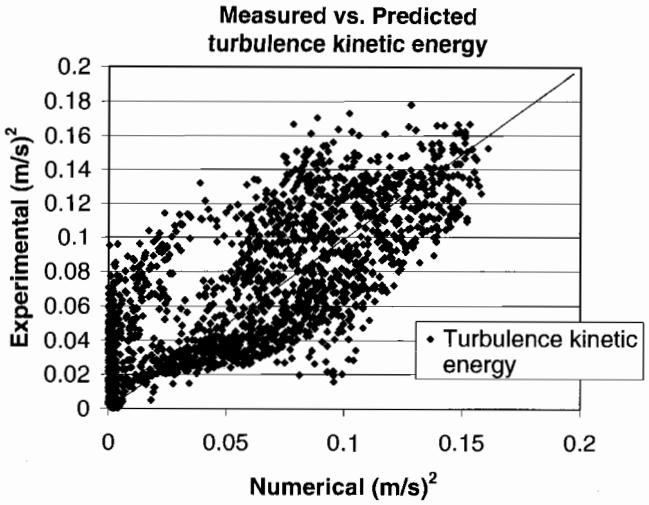

Fig. 10. Experimental vs. numerical results for turbulence kinetic energy.

Acknowledgements

This article was supported by Grant #1 R01 OH07363 from the National Institute for Occupational Safety and Health (NIOSH), Centers for Disease Control (CDC). Its contents are solely the responsibility of the authors and do not necessarily represent the official views of NIOSH.

References

Cadafalch, J., Perez-Segarra, C.D., Consul, R., Oliva, A., 2002. Verification of finite volume computations on steady-state fluid flow and heat transfer. ASME J. Fluids Eng. 124, 11–21.

Chandna, A., 1997. Flow past an elliptic cylinder. J. Comput. Appl. Math. 85 (2), 203–214.

Eisner, A.D., Heist, D.K., Drake, Z.E., Mitchell, W.J., Wiener, R.W., 2002. On the impact of the human (child) microclimate on passive aerosol monitor performance. Aerosol Sci. Technol. 37, 803–813.

Fluid Dynamics International, 1998. FIDAP Manual. Evanston, IL.

Flynn, M.R., Ljungqvist, B., 1995. A review of wake effects on worker exposure. Ann. Occup. Hyg. 39 (2), 211–221.

Flynn, M.R., Sills, E., 2000. On the use of computational fluid dynamics in the prediction and control of exposure to airborne contaminants—an illustration using spray painting. Ann. Occup. Hyg. 44 (3), 191–202.

Flynn, M.R., Sills, E., 2001. Numerical simulation of human exposure to aerosols generated during compressed air spray painting in cross-flow ventilated booths. ASME J. Fluids Eng. 123, 64–70.

Flynn, M.R., Chen, M., Kim, T., Muthedath, P., 1995. Computational simulation of worker exposure using a particle trajectory method. Ann. Occup. Hyg. 39 (3), 277–289.

Heinonen, K., Kulmala, I., Saamanen, A., 1996. Local ventilation for powder handling a combination of local supply and exhaust air. Am. Ind. Hyg. Assoc. J. 57, 356–365.

Heist, D.K., Richmond-Bryant, J., Eisner, A., Conner, T., 2003. Development of a versatile aerosol generating system for use in a large wind tunnel. Aerosol Sci. Technol. 37, 293–301.

Hyun, S., Kleinstreuer, C., 2002. Computational analysis of a human inhalation test chamber for dosimetry-and health effect studies. Appl. Occup. Environ. Hyg. 17 (8), 561–572.

Kim, T., Flynn, M.R., 1991. Modeling a worker's exposure from a hand-held source in a uniform freestream. Am. Ind. Hyg. Assoc. J. 52 (11), 458–463.

Kim, T., Flynn, M.R., 1995. Numerical simulation of airflow around multiple objects using the discrete vortex method. J. Wind Eng. Ind. Aerodyn. 56 (2,3), 213–234.

Kondjoyan, A., Daudin, D., 1995. Effects of freestream turbulence intensity on heat and mass transfers at the surface of a circular cylinder and an elliptical cylinder, axis ratio 4. Int. J. Heat Mass Transfer 38 (10), 1735–1749.

Kulmala, I., Saamanen, A., Enbom, S., 1996. The effect of contaminant source location on worker exposure in the near-wake region. Ann. Occup. Hyg. 40, 511–523.

Ma, X., Karamanos, G.-S., Karniadakis, G.E., 2000. Dynamics and low-dimensionality of a turbulent near wake. J. Fluid Mech. 410, 29–65.

Okamoto, S., Sunabashiri, Y., 1992. Vortex shedding from a circular cylinder of finite length placed on a ground plane. AIAA J. 114, 512–521.

Park, C.-W., Lee, C.-J., 2000. Free end effects on the near wake flow structure behind a finite circular cylinder. J. Wind Eng. Ind. Aerodyn. 88, 231–246.

Richmond-Bryant, J., 2003. Verification testing in computational fluid dynamics: an example using Reynolds averaged Navier–Stokes methods for two-dimensional flow in the near wake of a circular cylinder. Int. J. Numer. Methods Fluids 43, 1371–1389.

Roache, P.J., 1998. Verification and Validation in Computational Science and Engineering. Hermosa Publishers, Albuquerque, NM.

Sokal, R.R., Rohlf, F.J., 1981. Biometry, 2nd Edition. W.H. Freeman and Co., San Francisco, CA.

Stern, F., Wilson, R., Coleman, H.W., Paterson, E.G., 2001. Comprehensive approach to verification and validation of CFD simulations—Part 1: methodology and procedures. ASME J. Fluids Eng. 123, 793–802.

Tanaka, S., Murata, S., 1999. An investigation of the wake structure and aerodynamic characteristics of a finite circular cylinder. JSME Int. J. Series B 42 (2), 178–187.